



Characterization and Bias-Correction of Low-Level Jets at FINO1 Using LiDAR Observations and Reanalysis Data

Hai Bui¹, Mostafa Bakhoday-Paskyabi¹, and Joachim Reuder¹

¹Geophysical Institute and Bergen Offshore Wind Centre, University of Bergen, Norway

Correspondence: Hai Bui (hai.bui@uib.no)

Abstract. Low-level jets (LLJs) are wind maxima typically observed within a few hundred meters of the surface. They are often associated with high vertical wind shear, which significantly impacts the performance and loading of modern wind turbines. In this study, we characterize LLJs over the North Sea using one year of LiDAR observations from FINO1 (2015–2016) and compare them with reanalysis (ERA5) and hindcast (NORA3) data. We introduce a log-jet fitting method to represent each
5 observed or modeled wind profile with five parameters, enabling a direct comparison between LiDAR and model data. Results show that strong LLJs are generally underestimated by reanalysis and hindcast products. A bias-correction procedure based on quantile mapping is then applied to a 50-year ERA5 dataset to improve the long-term representation of LLJs. K-means clustering further reveals distinct directional and stability-dependent LLJ patterns. The findings highlight the need for detailed modeling of near-surface wind structures and motivate future numerical simulations to clarify the underlying mechanisms that
10 govern LLJ development and variability.

1 Introduction

Low-Level Jets (LLJs) are significant atmospheric phenomena characterized by strong wind speed maxima occurring within the lower part of the atmospheric boundary layer. They play a crucial role in various meteorological and climatological processes, including the transport of moisture, heat, and momentum, and are of particular interest for offshore wind energy applications
15 due to their influence on wind power generation and structural loading (Gutierrez et al., 2016, 2017; Gadde and Stevens, 2021; Pichugina et al., 2017; Aird et al., 2022). Their high wind speeds and large shear gradients can have substantial implications for modern wind turbines, which sweep rotor areas extending up to and beyond 200 m in height. Consequently, understanding the occurrence, intensity, and variability of LLJs is essential for accurate resource assessment, turbine design, and operational forecasting.

20 Reanalysis datasets, such as ERA5 (Hersbach et al., 2020) and hindcast datasets like NORA3 (Haakenstad et al., 2021), offer valuable resources for studying LLJs by offering comprehensive spatial and temporal coverage. These datasets have been used in several studies to investigate LLJ characteristics both globally and regionally (e.g., Kalverla et al., 2019; Lima et al., 2022; Hallgren et al., 2020; Luiz and Fiedler, 2024). Despite their strengths, biases in reanalysis and hindcast data often limit their accuracy in reproducing specific LLJ features, including their intensity, frequency, and vertical placement. The relatively
25 high spatial resolution of NORA3 (3 km) is beneficial for boundary-layer wind fields (Solbrekke et al., 2021), yet each model



run spans only 9 hours, which may not fully capture the entire inertial oscillation period of roughly 17 hours at mid-latitudes (Blackadar, 1957). Furthermore, parameterization schemes for boundary-layer processes can introduce additional errors in LLJ representations (Smith et al., 2018; Nunalee and Basu, 2014; Paskyabi et al., 2020).

Observations that measure vertical wind profiles, such as radiosondes and LiDAR, are crucial for validating and improving model-based LLJ analyses and simulations (Wagner et al., 2019; Kalverla et al., 2019; Rubio et al., 2022; Bakhoday-Paskyabi and Flügge, 2021). Radiosondes typically have limited temporal resolution (often just two launches per day), which constrains their utility for studying transient LLJ events. By contrast, LiDAR systems provide high-resolution data both temporally and vertically, making them particularly useful for detecting and characterizing LLJs. However, continuous, long-term LiDAR datasets spanning multiple years remain relatively rare, especially in offshore environments.

In this study, we focus on two widely used reanalysis/hindcast datasets, ERA5 (Hersbach et al., 2020) and NORA3 (Haakenstad et al., 2021), and compare their LLJ representations with high-resolution LiDAR observations from the FINO1 offshore platform. Both datasets provide extensive spatial coverage and generally show good agreement with offshore measurements (Cheynet et al., 2024). However, previous comparisons against LiDAR data have revealed a systematic underestimation of strong LLJs in these reanalyses (Kalverla et al., 2019; Lima et al., 2022). To leverage their long temporal spans while correcting for bias, the observations can be used to adjust the datasets accordingly. In a first step we introduce a novel *log-jet decomposition* method, with the aim to systematically assess LLJ characteristics and their representation in models. This approach partitions the wind profile into two components: a near-surface logarithmic portion, where wind speed increases monotonically with height, and a jet component capturing the local wind maximum that defines the LLJ. By focusing on these LLJ-specific parameters, the method provides a straightforward way to isolate and quantify biases in ERA5 and NORA3. To improve the LLJ representation in ERA5 over a multi-decade period, we apply in a second step a quantile-mapping bias correction to the log-jet parameters. This decomposition produces five parameters that characterize the wind profile, each of which is corrected via quantile mapping to align ERA5 distributions with LiDAR observations (Costoya et al., 2020; Benetazzo et al., 2022). The resulting bias-corrected ERA5 dataset more accurately captures both the intensity and frequency of LLJs at FINO1. Finally, we apply a clustering algorithm to categorize the corrected LLJs into distinct groups based on wind profiles and stability properties, assessing their frequency and associated synoptic conditions. This offers deeper insights into the variability of these jets and their links to different atmospheric drivers.

Overall, this paper aims to bridge the gap between model-based and observation-based LLJ analyses in offshore environments, with implications for wind energy resource assessment, turbine load estimation, and operational forecasting. The findings underscore the need for both high-quality observational data and targeted numerical modeling efforts to capture the complex dynamics of marine boundary layers. Furthermore, our results motivate additional numerical simulations to clarify the physical mechanisms driving LLJ formation and variability, ultimately contributing to improved forecasting and modeling capabilities for offshore wind energy applications.

This paper is organized as follows: Section 2 describes the datasets and the methodologies employed, including the log-jet decomposition, bias correction, and clustering techniques. Section 3 presents the evaluation of model data against LiDAR ob-



60 servations, the climatology of bias-corrected LLJs, and the characteristics of distinct LLJ clusters. Finally, Section 4 discusses the implications of these findings and offers concluding remarks.

2 Data and Methods

2.1 LiDAR Observations and Model Datasets

In this study, we use LiDAR observations collected the OBLEX-F1 campaign at the FINO1 offshore platform, conducted
65 between May 2015 and September 2016 (Cherukuru et al., 2017; Krishnamurthy et al., 2017). These profiles extend from 72 m up to 3126 m above mean sea level, with a vertical resolution of 23.5 m. For our analysis, we concentrate on the lower portion of the wind profile, specifically up to around 1 km, where data coverage is more reliable and pertinent to boundary layer dynamics.

For comparison, we utilize data from ERA5, the fifth-generation European Reanalysis from the European Centre for Medium-
70 Range Weather Forecasts (ECMWF) (Hersbach et al., 2020). ERA5 is a widely used global climate reanalysis dataset, known for its improved modelling and data assimilation techniques compared to its predecessor, ERA-Interim. It provides hourly estimates of a vast number of weather and climate related variables. The 3D data is available on 137 vertical levels and with a horizontal grid spacing of 0.28125° (approximately 31 km) (Hersbach et al., 2020). In this study, we extract wind profiles, including zonal and meridional wind components, alongside potential temperature, from the ERA5 grid cell closest to the FINO1
75 location. Given our focus on the lower atmospheric boundary layer and LLJ structures, we limit our data retrieval to the 18 lowest model levels, extending up to approximately 800 m. This selection offers a balance between computational efficiency and sufficient vertical resolution for our objectives.

Additionally, we use NORA3, which is a nonhydrostatic 3-km hindcast dataset for the North Sea, the Norwegian Sea, and the Barents Sea (Haakenstad et al., 2021). The dataset was generated using the non-hydrostatic convection-permitting
80 numerical weather prediction HARMONIE-AROME (Bengtsson et al., 2017), forced at the lateral boundaries by ERA5 data. It is initialized four times daily, each run producing 9-hour forecasts. NORA3 data is available at 3-hour intervals on all 65 model levels, or at hourly intervals on a reduced set of seven height levels below 750 m. For this research, we opt for the hourly subset at the grid point nearest to FINO1. This choice prioritizes higher temporal resolution within the marine boundary layer, which is crucial for capturing the dynamics of transient events such as LLJs. All wind profiles from LiDAR, NORA3,
85 and ERA5 are vertically interpolated to a common grid to ensure comparability across the datasets. This grid spans from 80 m to 740 m in 20-m increments, covering the primary region of interest for boundary layer and LLJ analysis. Furthermore, the LiDAR data are temporally aggregated to an hourly resolution to match the temporal resolution of the NORA3 hourly subset and to facilitate direct comparisons.

Figure 1 presents an example of processed wind speed profiles in form of time-height cross-sections derived from the
90 three datasets, spanning 12-14 August 2015. This period was specifically chosen to illustrate a prominent LLJ event, which is distinctly observed in the LiDAR data, exhibiting a peak wind speed at approximately 300 m near midnight on 13 August. While both ERA5 and NORA3 capture the overall wind speed trend, including the LLJ structure, they exhibit a slight underestimation

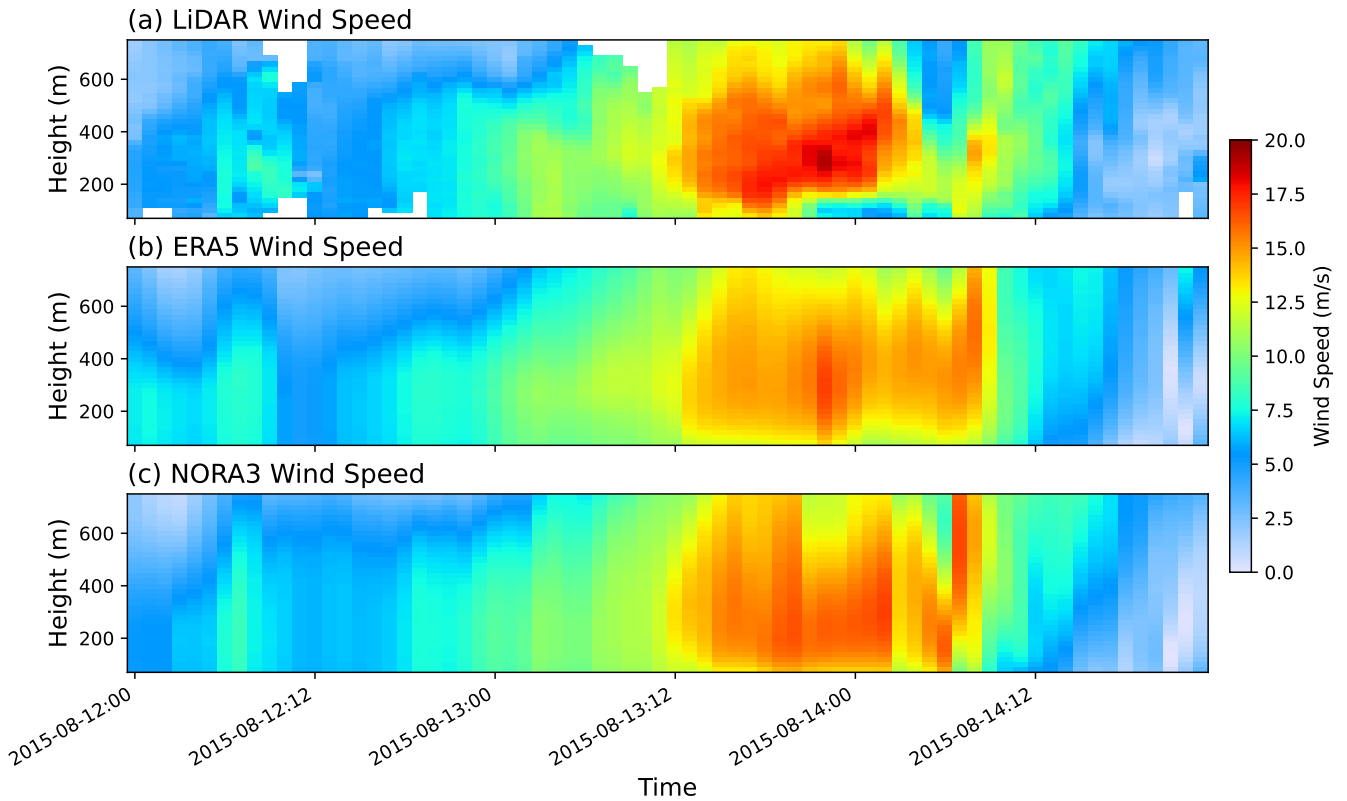


Figure 1. Time-height cross-section of wind speed at FINO1 from different data sources from 12 to 14 August 2015. (a) LiDAR observations, (b) ERA5 reanalysis, and (c) NORA3 hindcast.

of the maximum LLJ wind speeds compared to the LiDAR observations. Furthermore, the LiDAR data reveals a low wind speed anomaly below 200 m, commencing in the evening of 13 August, which is attributed to the wake effect from the Alpha Ventus
 95 wind farm in the vicinity of the FINO1 platform, as documented by (Bui et al., 2024).

To investigate the climatological characteristics of LLJs, we analyze a continuous 50-year dataset of 1-hourly ERA5 wind profiles, spanning from 1971 to 2020. For composite analyses focused on larger-scale atmospheric patterns, we additionally extract two-dimensional fields of geopotential height and horizontal wind components at the 975 hPa and 500 hPa pressure levels from ERA5. These synoptic-scale variables are used to examine the broader atmospheric environment associated with
 100 each detected LLJ event, helping to elucidate the synoptic drivers and their effect on the characteristics and variability of offshore LLJs.

2.2 Low-level jet detection and characterization

The general definition of an LLJ remains loosely defined, typically referring to a wind speed maximum within the lowest few kilometers of the atmosphere (Stensrud, 1996), and there is no universal established method or set of criteria for LLJ

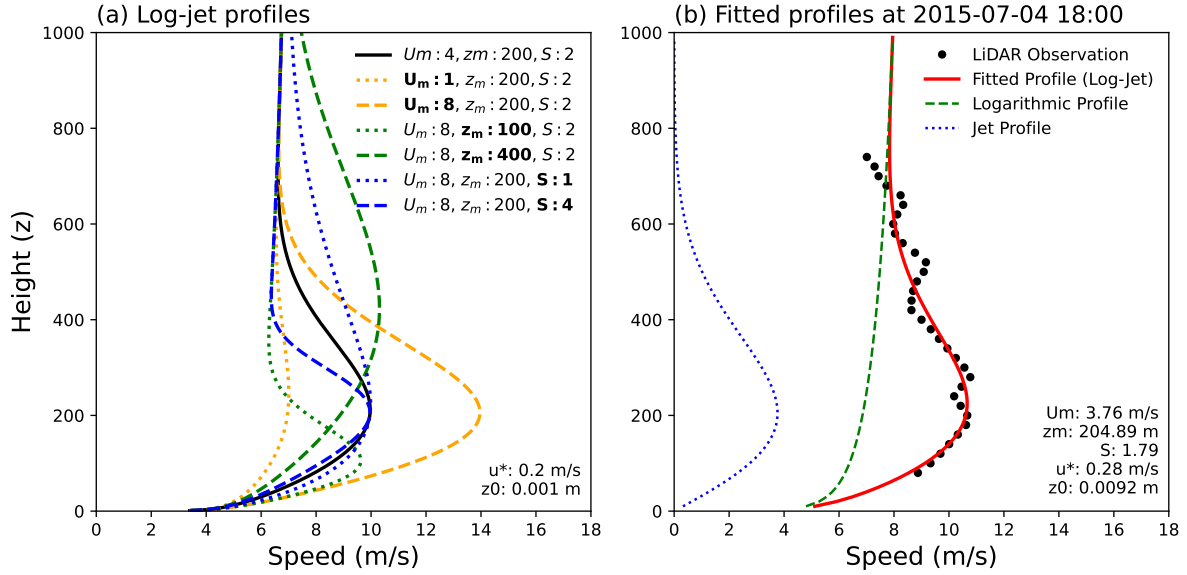


Figure 2. (a) Idealized log-jet profiles illustrating the effect of varying jet parameters. (b) Fitted profiles for LiDAR observations at 18:00 on 2015-07-04, with the logarithmic and jet components displayed separately.

105 detection (Hallgren et al., 2023). One widely used metric in previous studies is the wind speed fall-off, defined as the difference between the wind speed maximum and the minimum above it where different studies apply either an absolute or relative fall-off threshold. The absolute fall-off threshold typically ranges from 2 to 5 m s^{-1} (Nunalee and Basu, 2014; Kalverla et al., 2019; Hallgren et al., 2020; Carroll et al., 2019), while the relative fall-off threshold varies between 10% and 25% (Wagner et al., 2019; Baas et al., 2009; Kalverla et al., 2019; McCabe and Freedman, 2023; Aird et al., 2021). Some studies combine both
 110 absolute and relative thresholds (Wagner et al., 2019; McCabe and Freedman, 2023). The rationale for using a relative threshold is that it helps identify the characteristic nose shape of LLJs, while a weak absolute threshold (e.g., 2 m s^{-1}) helps filter out spurious LLJ detections caused by small errors when wind speeds are low. The detection height, which can range from a few hundred meters to 2 km, also influences LLJ identification (Kalverla et al., 2019). If the wind speed minimum above the jet maximum is higher than the predefined detection height, the wind speed at the top level is used instead, generally resulting in
 115 a lower fall-off ratio for higher-altitude LLJs.

In this study, we adopt a relative fall-off threshold of 20%, following (Wagner et al., 2019; Baas et al., 2009; Aird et al., 2021). However, before applying this threshold, we fit the wind profile $U(z)$ using the sum of a logarithmic profile and a jet component:

$$U_{\text{fitted}}(z) = U_{\text{log}}(z) + U_{\text{jet}}(z) \quad (1)$$



120 where

$$U_{\log}(z) = \frac{u_*}{\kappa} \log\left(\frac{z}{z_0}\right), \quad (2)$$

is a logarithmic profile. Here, $\kappa = 0.41$ is the von Kármán constant. The friction velocity u_* (m s^{-1}) and the roughness length z_0 are the fitting parameters to be estimated.

The second term represents a jet profile, defined by three parameters characterizing the LLJs:

$$125 \quad U_{\text{jet}}(z) = U_m \frac{z}{z_m} \exp\left\{\frac{1}{S} \left[1 - \left(\frac{z}{z_m}\right)^S\right]\right\}. \quad (3)$$

U_m represents the maximum wind speed, z_m , the height at which this maximum occurs, and S a shape parameter, defining the vertical structure and extension of the jet component (see Fig. 2a). This formulation is adapted from the tangential wind profile model for tropical cyclones proposed by DeMaria (1987).

The five log-jet parameters are determined by minimizing the mean squared error between the approximated profile and
 130 the original data. This decomposition method offers several advantages for LLJ analysis. First, it effectively filters out minor wind speed variations, isolating the primary jet structure (see Fig. 2b). Second, it facilitates gap-filling by addressing common LiDAR data gaps (e.g., Fig. 1), thereby enabling wind profile extrapolation across the full range. Third, it permits direct comparison of LLJ characteristics across datasets via the three key jet component parameters. Finally, a bias correction can be applied directly to the five parameters to align model data with observations. This bias correction can then be extended to
 135 longer reanalysis datasets to quantify LLJ characteristics over extended periods.

2.3 Bias Correction via Quantile Mapping

The log-jet decomposition was carried out for all three datasets, resulting in five time series of log-jet fitted parameters for each dataset. We then developed a quantile mapping procedure to bias-correct a 50-year ERA5 dataset (1971–2020). As shown in a later section, ERA5 data is comparable to or better than NORA3 for this specific location, making it a suitable choice due
 140 to its long historical record and ease of access. For each parameter, 100 percentiles were calculated and stored for use in the quantile mapping process (see Fig. 3a). However, due to the limited number of ERA5-LiDAR data pairs, using the raw data directly could lead to overfitting, resulting in an adjusted distribution with unrealistically small variability (see Fig. 3b). To address this issue, we applied a kernel density estimation (KDE) smoothing step to mitigate sampling limitations in the LiDAR dataset. Specifically, we used an *ad hoc* KDE bandwidth of 0.2 for parameters U_m , z_m , and S , and 0.5 for parameters u^* and
 145 z_0 . These bandwidths are smaller than the default KDE values, ensuring that small variations in the final probability density function (PDF) are smoothed while preserving the overall shape of the distribution. Although the quantile-quantile plots in Fig. 3a appear visually similar for both the original and KDE-smoothed data, applying a relatively small bandwidth in the KDE step leads to noticeable differences in the final PDF (see Fig. 3b). This highlights the sensitivity of the histogram shape to the smoothing procedure, even when the corresponding quantile values differ only slightly.

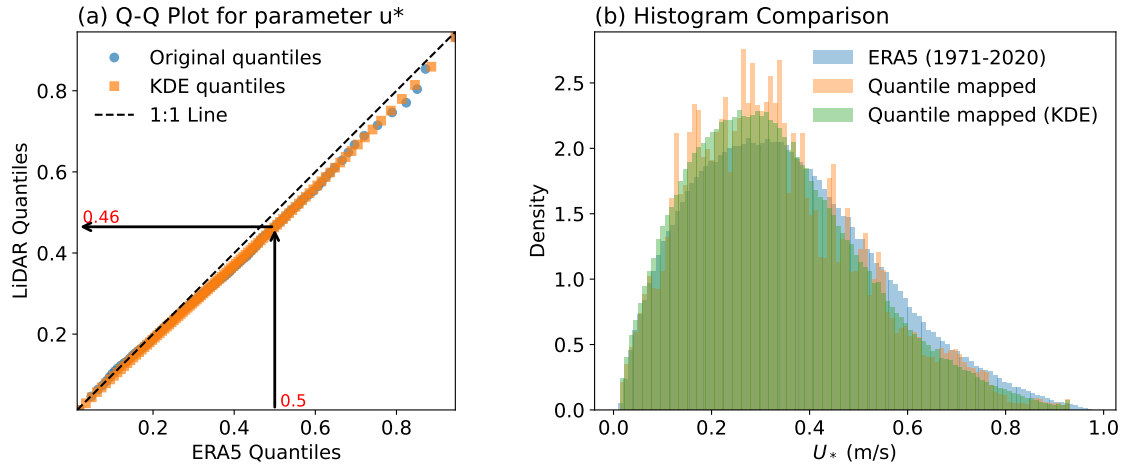


Figure 3. (a) Q–Q plot for parameter u^* comparing the original quantiles (orange circles) and the KDE-based quantiles (blue squares), with the dashed line indicating the 1:1 reference. The arrows illustrate how an ERA5 quantile (horizontal axis) maps to its corresponding a LiDAR quantile (vertical axis). (b) Histogram comparison of the ERA5 dataset (1971–2020), the quantile-mapped dataset with and without applying the KDE.

150 2.4 K-Means Clustering and Composite Analysis

After bias-correcting the 50-year ERA5 log-jet parameters using the quantile mapping method, wind profiles are reconstructed to facilitate LLJ detection. LLJs are identified using a 20% threshold for the fall-off rate.

The detected LLJs are then classified using the K-means method (MacQueen, 1967), a clustering algorithm that minimizes within-cluster variance. Clustering is performed on the horizontal wind components (U and V) across all vertical levels, thereby
 155 capturing the shape, magnitude, and direction of the entire wind profile for each cluster. To determine the optimal number of clusters, we apply the elbow method, which evaluates the total within-cluster sum of squares as a function of cluster count. A clear inflection point at three clusters suggests this number balances complexity and explanatory power.

To further account for the role of atmospheric stability, each of the three clusters is subdivided into two subclusters using the K-means method based on the vertical gradient of potential temperature in the lowest 300 m. This gradient serves as a proxy
 160 for stratification, which influences LLJ formation and persistence.

To investigate the large-scale weather patterns associated with each LLJ cluster, composite maps of wind speed and geopotential height at 925 hPa and 500 hPa are generated. Wind vectors are overlaid to visualize prevailing synoptic flow regimes.

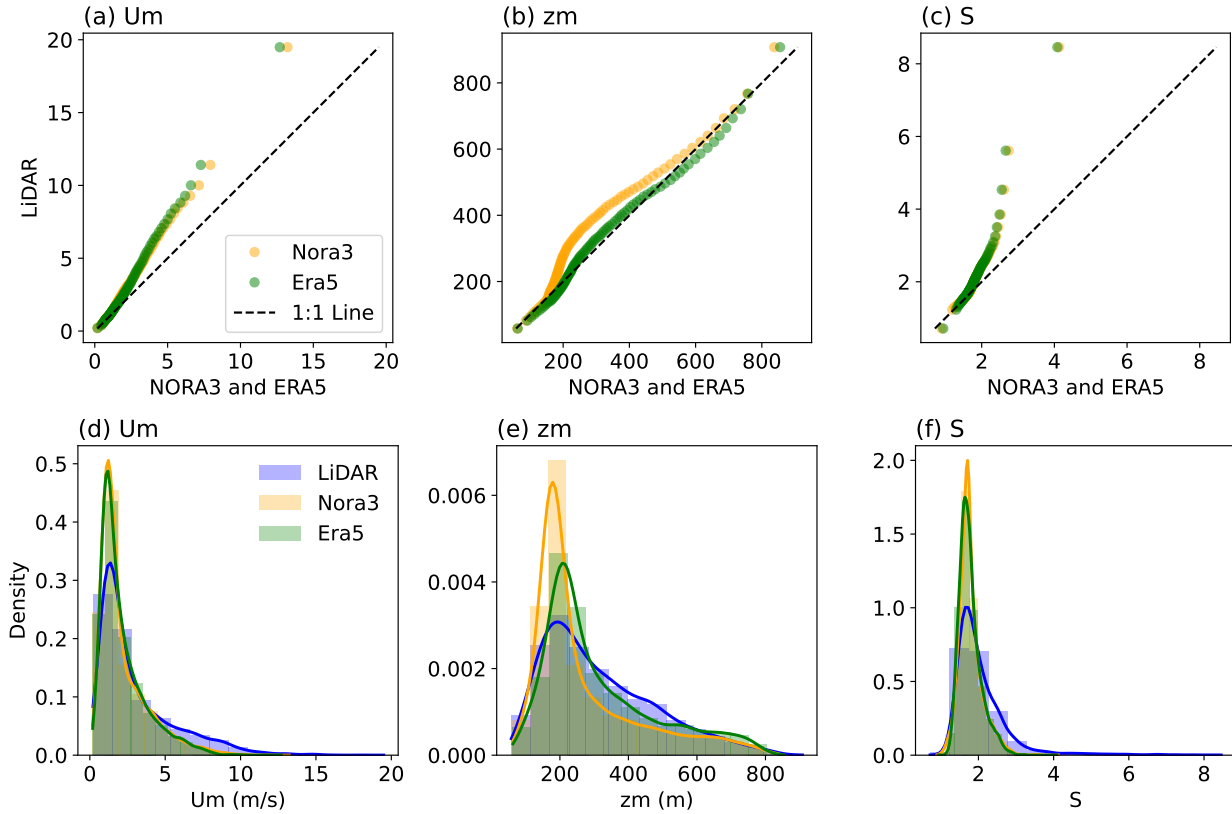


Figure 4. (a-c) Q–Q plots of model quantiles vs. LiDAR quantiles for U_m , z_m and S , respectively. (d-f) Normalized histograms (bars) with KDE overlays (solid lines) for the data from LiDAR, NORA3, and ERA5. The dashed black line in (a–c) indicates the 1:1 reference.

3 Results

3.1 Model Evaluation against LiDAR Observations

165 The log-jet decomposition enables a direct comparison of LLJ properties independent of the threshold used for LLJ detection.
 The quantile-quantile (Q–Q) plot and histogram of U_m (Fig. 4a, d) show that the distribution of U_m is surprisingly similar
 for NORA3 and ERA5. However, both datasets exhibit a systematic bias, as evidenced by their deviations from the 1:1 line.
 Specifically, these deviations increase at higher quantile levels. From the 0.6 quantile level (corresponding to a quantile value
 of 2 m/s) onward, both models consistently underestimate the LiDAR observations across all larger quantiles by approximately
 170 30%.

A similar conclusion can be drawn for the shape parameter S , where both reanalysis datasets tend to underestimate the
 LiDAR values. A larger S corresponds to a broader jet profile (see Fig. 2a), which results in a smaller fall-off rate. For both
 U_m and S , NORA3 quantiles are slightly closer to the LiDAR data compared to ERA5 (Fig. 4a, c) at larger values. However, at



lower values, ERA5 exhibits a marginally better agreement with the LiDAR, as indicated by the KDE plots (Fig. 4d, f). Overall, both reanalysis datasets display a similar underestimation of the two parameters in the fitted LLJ representation compared to the LiDAR observations, despite NORA3 being a high-resolution downscaling of ERA5.

For z_m , which represents the LLJ height, all three datasets show a peak in the distribution (Fig. 4e) at approximately 200 m. However, the two reanalysis datasets overestimate the frequency around this level while underestimating the frequency at higher altitudes. This discrepancy is less pronounced in ERA5 than in NORA3, as also indicated by the Q–Q plots (Fig. 4b), where the ERA5–LiDAR quantiles align more closely with the 1:1 reference line compared to NORA3–LiDAR.

Overall, ERA5 and NORA3 exhibit similar characteristics when compared to the LiDAR data: the frequency of strong jet magnitudes is underestimated, leading to lower LLJ frequencies and intensities. Additionally, ERA5 provides a closer match to the observed jet height distribution than NORA3. Thus, for the next sections, we apply quantile mapping to bias-correct the 50-year-long ERA5 dataset for characterizing the LLJs. This approach uses the observed distributions from the LiDAR data to adjust ERA5’s LLJ properties, ensuring a more reliable long-term analysis of LLJ behavior.

3.2 LLJ Climatology and Clustering for biased-corrected ERA5 data

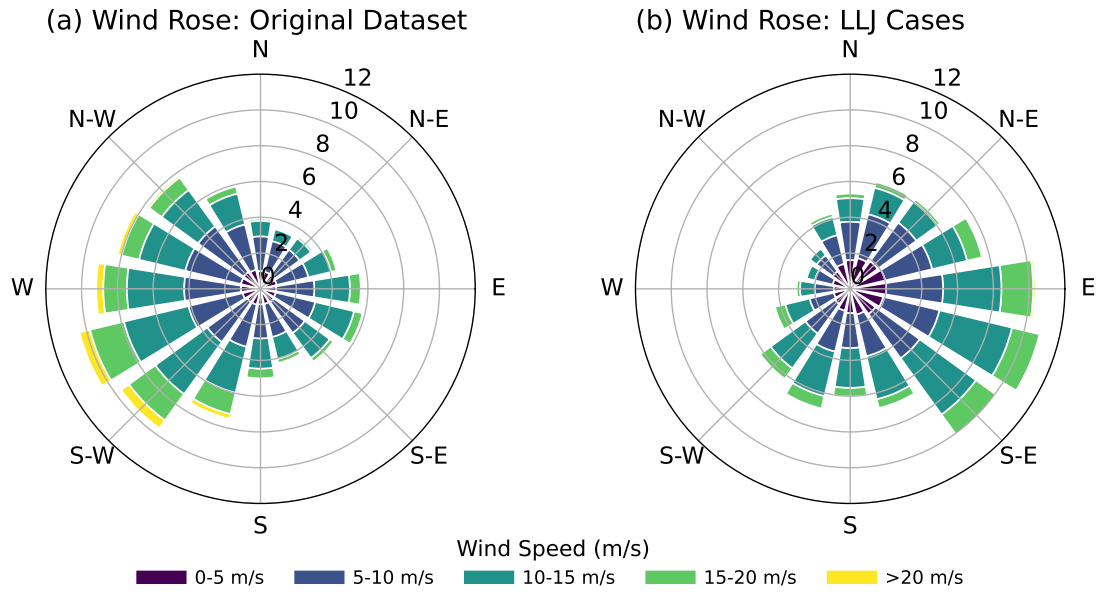


Figure 5. (a) Wind rose of the original ERA5 dataset at 200 m above ground, showing the distribution of wind directions (azimuth) and wind speeds (color bins). (b) Wind rose of the LLJ cases extracted from the same dataset, illustrating a subset of conditions where wind speeds and directions differ notably from the overall climatology.

After bias-correcting the log-jet parameters in the 50-year ERA5 dataset, the wind profiles were reconstructed and LLJs were identified using a 20% fall-off rate threshold. To illustrate the differences between the overall climatological wind conditions



and the conditions under LLJs, we present wind roses at 200 m above sea level—near the peak height of the LLJ distribution (Fig. 4e)—for the full dataset (Fig. 5a) and for the LLJ subset (Fig. 5b). In Fig. 5a, the prevailing winds are predominantly west-southwesterly, with mainly moderate speeds in the range of 5–15 m/s. The occurrence of higher wind speeds (15–20 m/s) is notable, though not dominant, and only a small fraction of winds exceed 20 m/s. By contrast, the LLJ subset (Fig. 5b) also features speeds primarily between 5–15 m/s but shows fewer occurrences of 15–20 m/s winds, and no LLJs exceed 20 m/s. Additionally, while the full dataset is characterized by a prevailing west-southwesterly direction, the LLJs are nearly reversed, predominantly blowing from the east-southeast. This directional shift highlights the distinct synoptic or local conditions under which LLJs form at a given site and underscores the importance of separately analyzing LLJ behavior for applications such as wind resource assessment or boundary-layer studies.

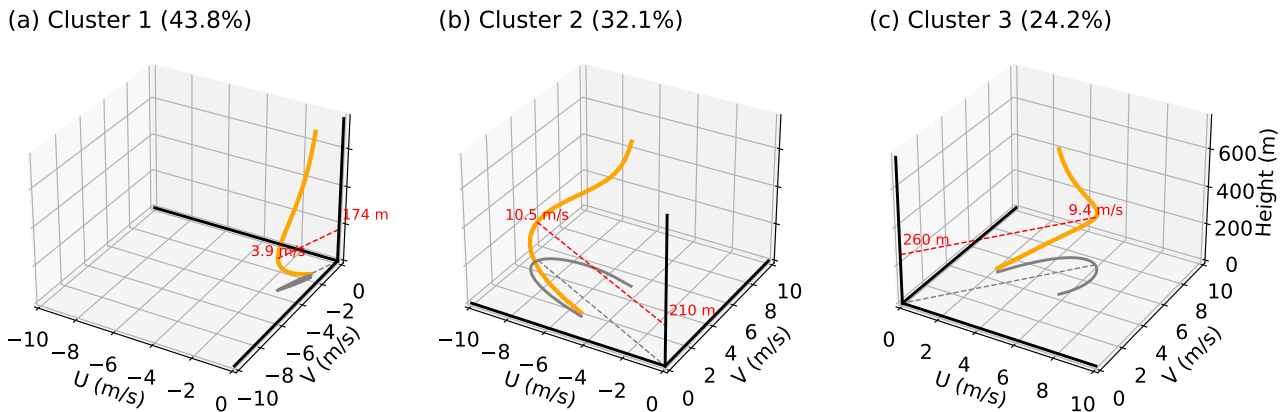


Figure 6. Three-dimensional hodographs of the average wind profiles for the three LLJ clusters. The orange lines represent the mean wind vector, while the thin gray lines on the bottom plane illustrate the horizontal wind projection.

Figure 6 presents three distinct wind-profile clusters identified using the K-means clustering method for the identified LLJs. Each cluster corresponds to a different prevalent wind regime, potentially associated with specific synoptic or mesoscale conditions. Cluster 1 (Fig. 6a) is characterized by a north-northeast wind direction and has the highest frequency of occurrence (43.8%). Cluster 2 (Fig. 6b) accounts for 32.1% of cases and exhibits an east-southeast wind direction. Cluster 3 (Fig. 6c) covers 24.2% of cases and is associated with a southwest wind direction. Cluster 1 is the weakest in strength, with an average wind profile peak of approximately 4 m/s, and at the lowest height of 174 m. In contrast, Clusters 2 and 3 display similar wind strengths, with average wind profile peaks around 10 m/s (10.5 m/s for Cluster 2 and 9.4 m/s for Cluster 3). Cluster 3 has a higher average LLJ height of 260 m compared to Cluster 2 of 210 m. Additionally, Clusters 2 and 3 exhibit notable wind veer, where the wind vector rotates clockwise with increasing height. In contrast, Cluster 1 shows minimal change in wind direction with height, maintaining a nearly uniform north-northeast orientation throughout its profile.

The inertial oscillation (Blackadar, 1957) is a key process in forming LLJs over flat surfaces. It is initiated when a stable inversion layer decouples the atmosphere from the surface. Once decoupling occurs, for example due to radiative cooling, the wind vectors rotate clockwise in the Northern Hemisphere, transitioning from sub-geostrophic to super-geostrophic states. This

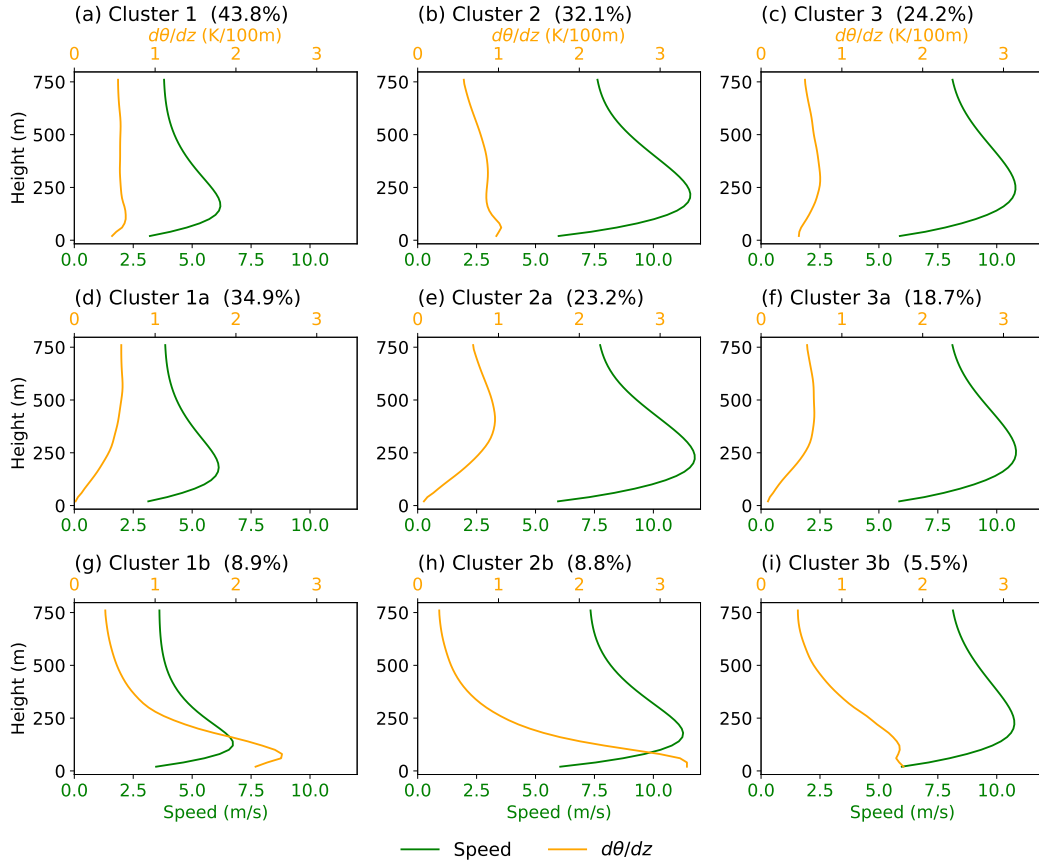


Figure 7. Average wind speed and vertical gradient of potential temperature ($d\theta/dz$) profiles for atmospheric clusters and sub-clusters.

transition can produce a wind speed maximum (i.e., the LLJ) above the inversion layer. To further understand LLJ formation, each group is subdivided using the K-means method applied to the vertical gradient of potential temperature, $d\theta/dz$, an indicator of atmospheric stability.

Figure 7 displays the vertical profiles of average wind speed and $d\theta/dz$ for the three clusters and their sub-clusters. Each primary cluster (Figs. 7a–c) is divided into two sub-clusters: *a* (middle row, Figs. 7d–f) and *b* (bottom row, Figs. 7g–i). Sub-cluster *a* represents a weakly stable condition, with $d\theta/dz$ near zero at the surface and increasing with height, while sub-cluster *b* is characterized by a stronger stable layer near the surface beneath the jet core. Overall, sub-cluster *a* comprises approximately 77% of the cases, whereas sub-cluster *b* accounts for the remaining 23%. In most instances (i.e. sub-cluster *a*), a strong inversion layer is absent below the LLJ core. In these cases, the trigger for inertial oscillation is not local; it is likely that the offshore location of FINO1 means the LLJ originates onshore and is subsequently advected offshore. Conversely, the pronounced inversion layer in sub-cluster *b* may be linked to radiative cooling of the sea surface or the advection of warmer air over the colder ocean.

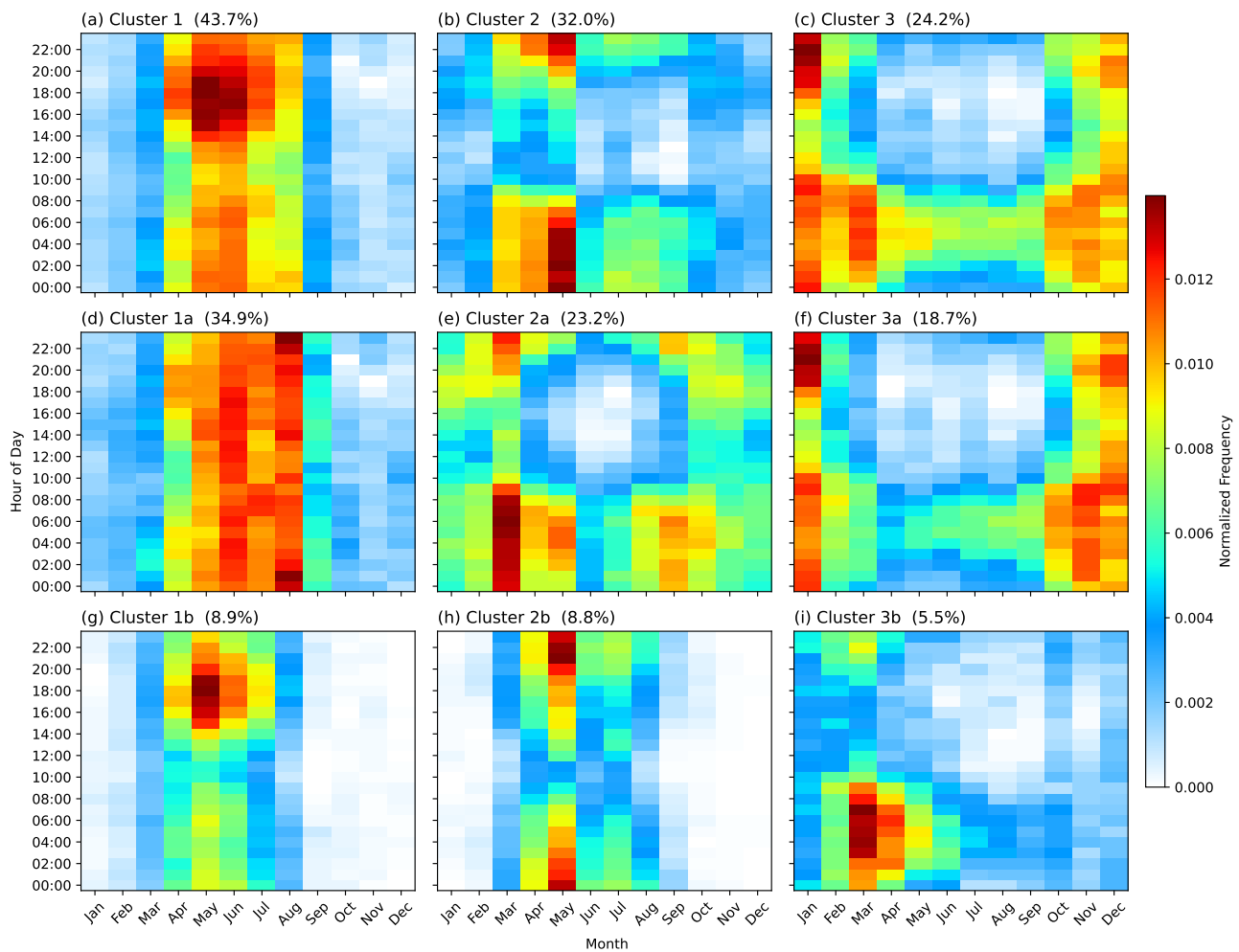


Figure 8. Temporal patterns of LLJ clusters and subclusters. The top row (a–c) shows the normalized frequency for the three main clusters, while the second (d–f) and third (g–i) rows display the normalized frequency for sub-clusters *a* and *b* respectively.



Figure 8 reveals distinct temporal signatures for each cluster and its sub-clusters. Cluster 1 (Fig. 8a) exhibits a strong annual cycle, with most LLJs occurring from February to August and peaking in May. A diurnal signal appears around 17:00 UTC, although LLJs can occur throughout the day. Notably, this diurnal peak is driven mainly by sub-cluster 1b (Fig. 8g), which shows a clear peak in the early evening (18:00–19:00 UTC). By contrast, sub-cluster 1a (Fig. 8d) lacks a strong diurnal pattern. Cluster 2 (Fig. 8b) also displays a clear annual cycle, with most LLJ activity from April to September. Its diurnal signal is stronger than that of Cluster 1, showing that most LLJs occur during the nighttime (18:00–08:00 UTC). Sub-cluster 2a (Fig. 8e) features a notable lack of LLJ events from May to September between 10:00 and 20:00 UTC, but otherwise LLJs can appear year-round. In contrast, sub-cluster 2b (Fig. 8h) has a pronounced annual cycle from March to August, similar to sub-cluster 1b, and exhibits a clear diurnal pattern peaking around 21:00–22:00 UTC, which is about three hours later than sub-cluster 2a. Cluster 3 (Fig. 8c) differs from Clusters 1 and 2 by occurring most frequently in winter, with a peak in January, and also shows a clear diurnal structure. Interestingly, there are two favored time windows: early morning (04:00–06:00 UTC) and early night (20:00–22:00 UTC). Sub-cluster 3a (Fig. 8f) largely mirrors the overall temporal pattern of Cluster 3. However, sub-cluster 3b (Fig. 8i) peaks in March, about two months earlier than sub-clusters 1b and 2b. Another notable difference is that while sub-clusters 1b and 2b peak before midnight, sub-cluster 3b reaches its maximum in the early morning (04:00–06:00 UTC). Overall, the *b*-type sub-clusters show stronger annual and diurnal signals than the *a*-type sub-clusters, typically featuring a well-defined nighttime peak characteristic of nocturnal LLJs. However, the differences in exact peak hours (e.g. early evening, near midnight, or early morning) hint at distinct underlying forcing mechanisms or meteorological conditions for each *b*-type sub-clusters.

3.3 Large-Scale Weather Patterns

To highlight the spatial patterns of each sub-cluster, Figure 9 shows the composite wind speed at 975 hPa (overlaid with wind vectors) for the six sub-clusters. sub-cluster 1a and 1b (Fig. 9a,d) features notably weaker wind speeds over most of the North Sea, with a modest southwesterly flow near the Dutch coast. By contrast, sub-clusters 2a and 2b (Fig. 9b,e) exhibits stronger southeasterly winds originating from the continent and blowing over the North Sea. Cluster 3a and 3b (Fig. 9c,f) is dominated by a pronounced southwesterly flow, which is essentially the opposite direction of cluster 1 but with higher wind speeds (often exceeding 10–12 m/s) and covering a broader area than the other clusters.

Figure 10 illustrates the composite geopotential height at 975 hPa, overlaid with wind vectors, for each sub-cluster. Cluster 1 (Fig. 10 a, d) is associated with weak pressure gradients near the FINO1 location. Sub-cluster 1a exhibits a southwest-northeast-oriented ridge, while in sub-cluster 1b, the FINO1 station lies within a high-pressure system. In both cases, the slope of the geopotential height surface (i.e., the density of the contours) is small, which corresponds to the weak wind speeds observed in Cluster 1. For Cluster 2 (Fig. 10b, e), the FINO1 station is positioned between a high-pressure system centered over the Baltic Sea and a low-pressure system to the east. Similarly, in Cluster 3 (Fig. 10 panels c, f), FINO1 is located between a high-pressure system to the southeast and a low-pressure system to the northeast. In all these cases, the geopotential height gradients are steeper than in Cluster 1, which explains the stronger wind speeds observed in Clusters 2 and 3.

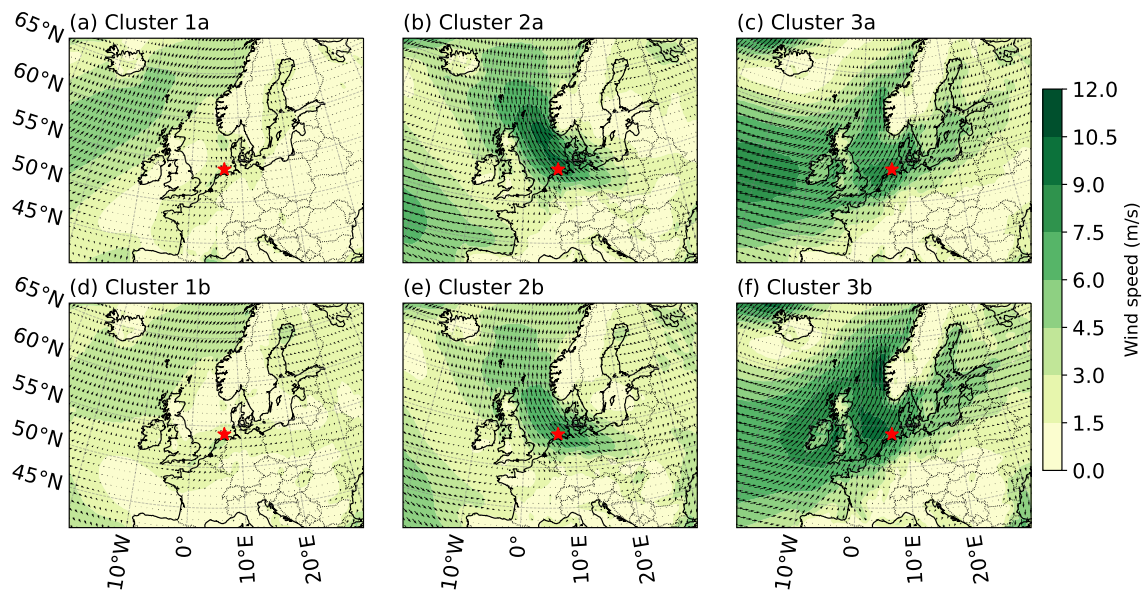


Figure 9. Composite wind speed (shading, in m/s) and wind vectors on the 975 hPa isobaric surface for six sub-clusters derived from ERA5 reanalysis. The red star marking the FINO1 offshore station.

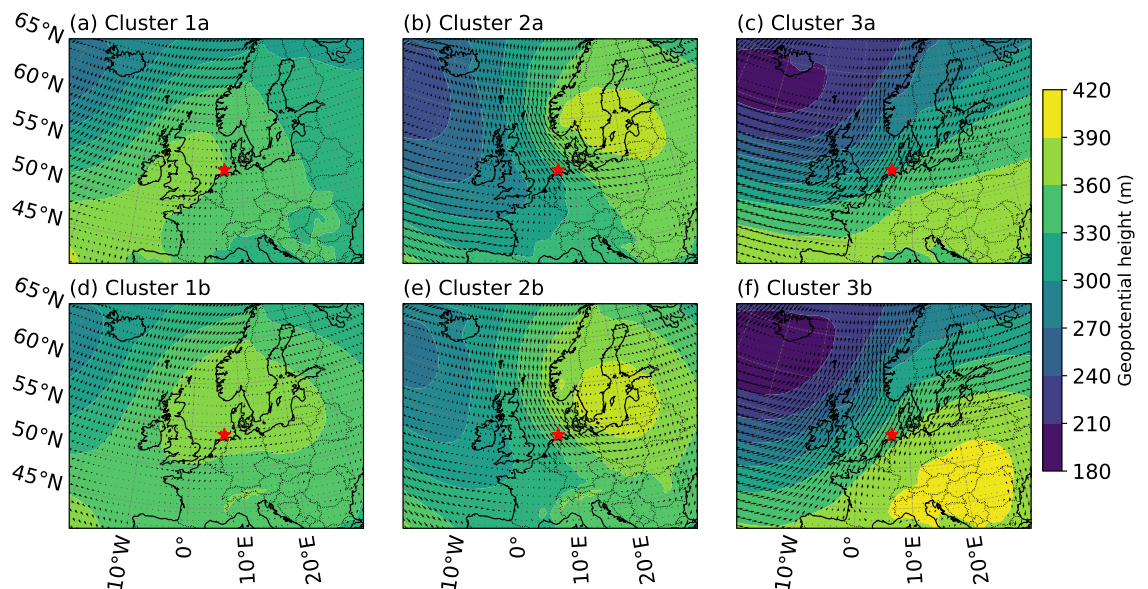


Figure 10. Composite geopotential height (shading, in meters) on 975 hPa isobaric surface for the same six subclusters as in Figure 7, derived from ERA5 reanalysis. The red star marks the location of the FINO1 offshore station.

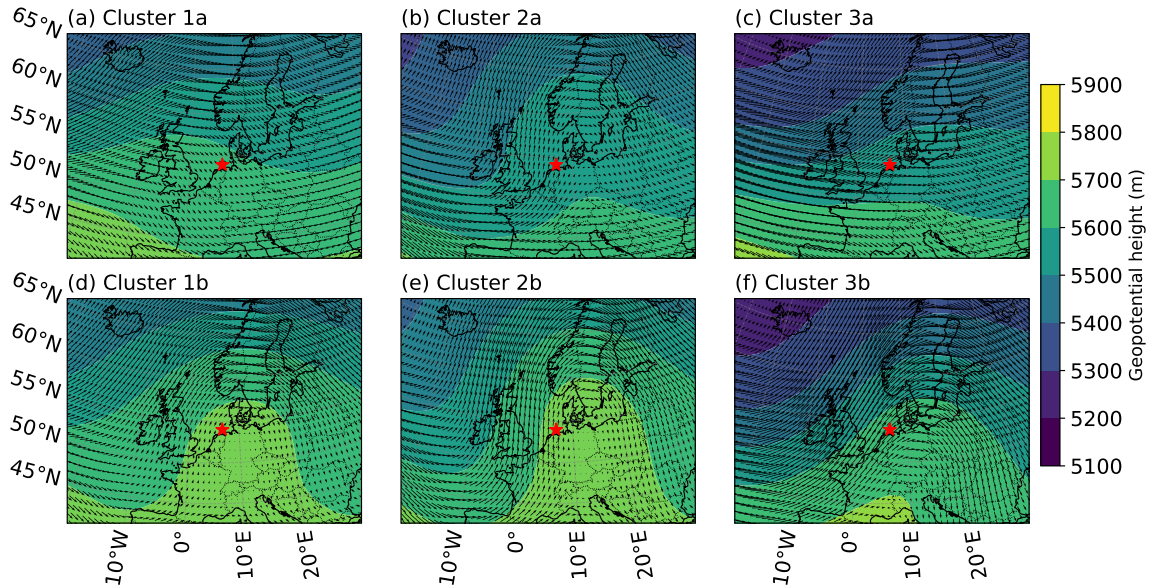


Figure 11. Similar to Fig. 10, but for 500-hPa isobaric surface.

The composite analysis of ERA5 geopotential height at the 500 hPa isobaric surface and wind vectors (Fig. 11) reveals distinct atmospheric regimes across the six subclusters, providing insight into the synoptic-scale flow patterns. In general, geopotential height increases toward the south, leading to a predominantly westerly flow. A ridge feature is evident over the FINO1 location in all cases, though its strength and structure differ between the subclusters. For subclusters 1a, 2a, and 3a (Fig. 11a–c), the ridge is less pronounced, and the height contours are more zonally oriented, indicating a relatively weak meridional pressure gradient. This results in lower wind speeds at this level. In contrast, for subclusters 1b, 2b, and 3b (Fig. 11d–f), the ridge is more sharply defined, with a stronger geopotential height gradient to the north, leading to enhanced westerly winds. A notable feature is the consistency in the 500-hPa geopotential patterns for the “b” sub-clusters. Despite the differences in surface-level structures observed in Fig. 10d–f, the geopotential height fields at 500 hPa remain relatively similar, with FINO1 consistently positioned on the western flank of a well-defined ridge centered near 10°E. This suggests that while surface-level variations exist, the upper-level forcing remains coherent.

4 Discussion and conclusion

This study presents a novel log–jet decomposition method for analyzing LLJs and applies it to compare reanalysis/hindcast datasets (ERA5 and NORA3) with LiDAR observations at the FINO1 offshore platform. The log–jet decomposition effectively separates the wind profile into a near-surface logarithmic component and a jet component, allowing for a more precise characterization of LLJ features. This method offers several advantages, including filtering out minor wind speed variations,



gap-filling in LiDAR data, direct comparison of LLJ characteristics across datasets, and facilitating bias correction of model data.

The comparison of ERA5 and NORA3 with LiDAR data reveals that both datasets tend to underestimate LLJ intensity and frequency. Surprisingly, ERA5 performs comparably to, or even slightly better than, NORA3 in representing LLJ characteristics at the FINO1 station, despite NORA3's higher spatial resolution (approximately 3 km) compared to ERA5. Several factors may contribute to this finding. First, NORA3, while having higher spatial resolution, may have fewer vertical layers than ERA5 in the boundary layer, potentially limiting its ability to resolve the vertical structure of LLJs. Second, NORA3 employs 9-hour integration runs, which may not fully capture the inertial oscillation period (approximately 17 hours at mid-latitudes), a crucial process in LLJ formation. Third, LLJs, while influenced by local factors, often have a relatively large spatial scale (e.g. see Fig. 9), suggesting that they may not be highly sensitive to the increased spatial resolution offered by NORA3, particularly in the offshore environment. It is important to note that this finding may be specific to offshore regions like FINO1. In onshore regions, where topography plays a more significant role, the higher resolution of NORA3 could potentially provide a greater advantage (Cheynet et al., 2024). Future studies should explore the performance of ERA5 and NORA3 in representing LLJs in coastal and onshore locations to assess the influence of topography and surface heterogeneity.

The temporal occurrence of LLJs, particularly the nocturnal LLJs associated with sub-cluster *b*, provides valuable insights into LLJ formation mechanisms. The presence of a low-level stable layer in these sub-clusters suggests a local mechanism for the initiation of inertial oscillation, driven by processes such as radiative cooling or the advection of warm air over a colder sea surface. However, the distinct peak times observed for different sub-clusters during the night (early evening, near midnight, and early morning) remain unclear. These differences may be related to the complex interplay between land-sea distribution, prevailing wind direction, and the timing of the development of the stable boundary layer. For instance, the orientation of the coastline relative to the wind direction could influence the advection of stable air and the subsequent development of nocturnal LLJs. To better understand these relationships and the reasons for model underestimation of observed LLJ characteristics, further numerical simulations, including idealized experiments and high-resolution simulations focused on specific LLJ events, are needed. These simulations should aim to resolve the relevant physical processes, such as boundary-layer dynamics, inertial oscillations, and the influence of land-sea contrasts, with greater accuracy.

This study demonstrates the value of combining high-resolution LiDAR observations with model-based datasets for understanding LLJs in offshore environments. The novel log-jet decomposition method provides a robust framework for analyzing LLJ characteristics and quantifying biases in reanalysis/hindcast data. The findings highlight the limitations of ERA5 and NORA3 in accurately representing LLJ intensity and frequency, underscoring the need for bias correction using observational data. The bias-corrected ERA5 dataset, combined with the LLJ clustering analysis, provides new insights into the variability of offshore LLJs and their associated synoptic conditions. The identification of distinct LLJ clusters with different temporal patterns and large-scale drivers contributes to a more comprehensive understanding of LLJ dynamics. The results have significant implications for offshore wind energy applications. Accurate characterization of LLJs is crucial for improving wind resource assessment, turbine design, and operational forecasting. The findings underscore the need for both high-quality observational data and targeted numerical modeling efforts to capture the complex dynamics of marine boundary layers. Future



research should focus on further refining numerical models to better represent LLJ formation and evolution, ultimately leading to improved forecasting and modeling capabilities for offshore wind energy applications.

310 *Code and data availability.* The ERA5 reanalysis data utilized in this study were obtained from the Copernicus Climate Change Service (C3S) Climate Data Store (CDS) at <https://cds.climate.copernicus.eu>. The NORA3 hindcast dataset is available from the Norwegian Meteorological Institute THREDDS server at <https://thredds.met.no/>. The processed log-jet parameters derived from ERA5, the bias-corrected parameters, the quantile mapping data are publicly available on Zenodo at <https://doi.org/10.5281/zenodo.15470418> (Bui, 2025).

315 *Author contributions.* Hai Bui conceptualized and designed the study, performed the data analysis, developed the necessary code, and wrote the original draft of the manuscript. Mostafa Bakhoday-Paskyabi and Joachim Reuder contributed to the discussion and refinement of the methodology, interpretation of the results, and critically reviewed and edited the manuscript.

Competing interests. The authors declare that they have no competing interests.

Acknowledgements. This study was supported by the Research Council of Norway (Norges forskningsråd) through the project ImpactWind SørVest (project number: 332034). The authors acknowledge the use of AI language models to assist in editing and refining the language of the manuscript.



320 References

- Aird, J. A., Barthelmie, R. J., Shepherd, T. J., and Pryor, S. C.: WRF-simulated low-level jets over Iowa: characterization and sensitivity studies, *Wind Energy Science*, 6, 1015–1030, 2021.
- Aird, J. A., Barthelmie, R. J., Shepherd, T. J., and Pryor, S. C.: Occurrence of low-level jets over the eastern US coastal zone at heights relevant to wind energy, *Energies*, 15, 445, 2022.
- 325 Baas, P., Bosveld, F., Klein Baltink, H., and Holtslag, A.: A climatology of nocturnal low-level jets at Cabauw, *Journal of Applied Meteorology and Climatology*, 48, 1627–1642, 2009.
- Bakhoday-Paskyabi, M. and Flügge, M.: Predictive capability of wrf cycling 3dvar: Lidar assimilation at fino1, in: *Journal of Physics: Conference Series*, vol. 2018, p. 012006, IOP Publishing, 2021.
- Benetazzo, A., Davison, S., Barbariol, F., Mercogliano, P., Favaretto, C., and Sclavo, M.: Correction of ERA5 wind for regional climate
 330 projections of sea waves, *Water*, 14, 1590, 2022.
- Bengtsson, L., Andrae, U., Aspelien, T., Batrak, Y., Calvo, J., de Rooy, W., Gleeson, E., Hansen-Sass, B., Homleid, M., Hortal, M., et al.: The HARMONIE–AROME model configuration in the ALADIN–HIRLAM NWP system, *Monthly Weather Review*, 145, 1919–1935, 2017.
- Blackadar, A. K.: Boundary layer wind maxima and their significance for the growth of nocturnal inversions, *Bulletin of the American
 335 Meteorological Society*, 38, 283–290, 1957.
- Bui, H., Bakhoday-Paskyabi, M., and Mohammadpour-Penchah, M.: Implementation of a Simple Actuator Disk for Large-Eddy Simulation in the Weather Research and Forecasting Model (WRF-SADLES v1. 2) for wind turbine wake simulation, *Geoscientific Model Development*, 17, 4447–4465, 2024.
- Bui, H. H.: Supplementary Data and Code for "Characterization and Bias-Correction of Low-Level Jets at FINO1 Using LiDAR Observations and Reanalysis Data", <https://doi.org/10.5281/zenodo.15470418>, 2025.
- 340 Carroll, B. J., Demoz, B. B., and Delgado, R.: An overview of low-level jet winds and corresponding mixed layer depths during PECAN, *Journal of Geophysical Research: Atmospheres*, 124, 9141–9160, 2019.
- Cherukuru, N. W., Calhoun, R., Krishnamurthy, R., Benny, S., Reuder, J., and Flügge, M.: 2D VAR single Doppler lidar vector retrieval and its application in offshore wind energy, *Energy Procedia*, 137, 497–504, 2017.
- 345 Cheynet, E., Diezel, J. M., Haakenstad, H., Breivik, Ø., Peña, A., and Reuder, J.: Tall Wind Profile Validation Using Lidar Observations and Hindcast Data, *Wind Energy Science Discussions*, 2024, 1–29, 2024.
- Costoya, X., Rocha, A., and Carvalho, D.: Using bias-correction to improve future projections of offshore wind energy resource: A case study on the Iberian Peninsula, *Applied Energy*, 262, 114 562, 2020.
- DeMaria, M.: Tropical cyclone track prediction with a barotropic spectral model, *Monthly weather review*, 115, 2346–2357, 1987.
- 350 Gadde, S. N. and Stevens, R. J.: Effect of low-level jet height on wind farm performance, *Journal of Renewable and Sustainable Energy*, 13, 2021.
- Gutierrez, W., Araya, G., Kiliyanpilakkil, P., Ruiz-Columbie, A., Tutkun, M., and Castillo, L.: Structural impact assessment of low level jets over wind turbines, *Journal of renewable and sustainable energy*, 8, 2016.
- Gutierrez, W., Ruiz-Columbie, A., Tutkun, M., and Castillo, L.: Impacts of the low-level jet's negative wind shear on the wind turbine, *Wind
 355 energy science*, 2, 533–545, 2017.



- Haakenstad, H., Breivik, Ø., Furevik, B. R., Reistad, M., Bohlinger, P., and Aarnes, O. J.: NORA3: A nonhydrostatic high-resolution hindcast of the North Sea, the Norwegian Sea, and the Barents Sea, *Journal of Applied Meteorology and Climatology*, 60, 1443–1464, 2021.
- Hallgren, C., Arnqvist, J., Ivanell, S., Körnich, H., Vakkari, V., and Sahlée, E.: Looking for an offshore low-level jet champion among recent reanalyses: a tight race over the Baltic Sea, *Energies*, 13, 3670, 2020.
- 360 Hallgren, C., Aird, J. A., Ivanell, S., Körnich, H., Barthelmie, R. J., Pryor, S. C., and Sahlée, E.: Brief communication: On the definition of the low-level jet, *Wind Energy Science*, 8, 1651–1658, 2023.
- Hersbach, H., Bell, B., Berrisford, P., Hirahara, S., Horányi, A., Muñoz-Sabater, J., Nicolas, J., Peubey, C., Radu, R., Schepers, D., et al.: The ERA5 global reanalysis, *Quarterly Journal of the Royal Meteorological Society*, 146, 1999–2049, 2020.
- Kalverla, P. C., Duncan Jr, J. B., Steeneveld, G.-J., and Holtslag, A. A.: Low-level jets over the North Sea based on ERA5 and observations: together they do better, *Wind Energy Science*, 4, 193–209, 2019.
- 365 Krishnamurthy, R., Reuder, J., Svandal, B., Fernando, H. J. S., and Jakobsen, J. B.: Offshore wind turbine wake characteristics using scanning Doppler lidar, *Energy Procedia*, 137, 428–442, 2017.
- Lima, D. C., Soares, P. M., Nogueira, M., and Semedo, A.: Global coastal low-level wind jets revisited through the new ERA5 reanalysis, *International Journal of Climatology*, 42, 4491–4507, 2022.
- 370 Luiz, E. W. and Fiedler, S.: Global climatology of low-level-jets: Occurrence, characteristics, and meteorological drivers, *Journal of Geophysical Research: Atmospheres*, 129, e2023JD040 262, 2024.
- MacQueen, J.: Some methods for classification and analysis of multivariate observations, in: *Proceedings of the Fifth Berkeley Symposium on Mathematical Statistics and Probability*, Volume 1: Statistics, vol. 5, pp. 281–298, University of California press, 1967.
- McCabe, E. J. and Freedman, J. M.: Development of an objective methodology for identifying the sea-breeze circulation and associated low-level jet in the New York Bight, *Weather and Forecasting*, 38, 571–589, 2023.
- 375 Nunalee, C. G. and Basu, S.: Mesoscale modeling of coastal low-level jets: implications for offshore wind resource estimation, *Wind Energy*, 17, 1199–1216, 2014.
- Paskyabi, M. B., Bui, H., and Penchah, M. M.: Atmospheric-Wave Multi-Scale Flow Modelling, Tech. Rep. D2.1, European Union’s Horizon 2020 Research and Innovation Program, <https://www.hiperwind.eu/publications>, deliverable under Grant Agreement No. 101006689, 2020.
- 380 Pichugina, Y., Brewer, W., Banta, R., Choukulkar, A., Clack, C., Marquis, M., McCarty, B., Weickmann, A., Sandberg, S., Marchbanks, R., et al.: Properties of the offshore low level jet and rotor layer wind shear as measured by scanning Doppler Lidar, *Wind Energy*, 20, 987–1002, 2017.
- Rubio, H., Kühn, M., and Gottschall, J.: Evaluation of low-level jets in the southern Baltic Sea: a comparison between ship-based lidar observational data and numerical models, *Wind Energy Science Discussions*, 2022, 1–29, 2022.
- 385 Smith, E. N., Gibbs, J. A., Fedorovich, E., and Klein, P. M.: WRF Model study of the Great Plains low-level jet: Effects of grid spacing and boundary layer parameterization, *Journal of Applied Meteorology and Climatology*, 57, 2375–2397, 2018.
- Solbrekke, I. M., Sorteberg, A., and Haakenstad, H.: The 3 km Norwegian reanalysis (NORA3)—a validation of offshore wind resources in the North Sea and the Norwegian Sea, *Wind Energy Science*, 6, 1501–1519, 2021.
- 390 Stensrud, D. J.: Importance of low-level jets to climate: A review, *Journal of Climate*, pp. 1698–1711, 1996.
- Wagner, D., Steinfeld, G., Witha, B., Wurps, H., and Reuder, J.: Low level jets over the southern North Sea, 2019.